

## Electrochemical Stability of Elemental Metal Nanoparticles

Lei Tang,<sup>†</sup> Xiaoqian Li,<sup>†</sup> Robert C. Cammarata,<sup>‡</sup> Cody Friesen,<sup>†</sup> and Karl Sieradzki\*,<sup>†</sup>

*Arizona State University, Tempe, Arizona 85287-8706, and Johns Hopkins University, Baltimore, Maryland 21218*

Received May 21, 2010; E-mail: karl.sieradzki@asu.edu

**Abstract:** The corrosion behavior of nanometer-scale solids is important in applications ranging from sensing to catalysis. Here we present a general thermodynamic analysis of this for the case of elemental metals and use the analysis to demonstrate the construction of a particle-size-dependent potential–pH diagram for the case of platinum. We discuss the data set required for the construction of such diagrams in general and describe how some parameters are accessible via experiment while others can only be reliably determined from first-principles-based electronic structure calculations. In the case of Pt, our analysis predicts that particles of diameter less than ~4 nm dissolve via the direct electrochemical dissolution pathway,  $\text{Pt} \rightarrow \text{Pt}^{2+} + 2\text{e}^-$ , while larger particles form an oxide. As an extension of previously published work by our group, electrochemical scanning tunneling microscopy is used to examine the stability of individual Pt-black particles with diameters ranging from 1 to 10 nm. Our experimental results confirm the thermodynamic predictions, suggesting that our analysis provides a general framework for the assessment of the electrochemical stability of nanoscale elemental metals.

Metal particles, wires, and thin films at nanometer length scales can have structural and electronic properties that differ from those of their bulk macroscopic counterparts. Our focus on the electrochemical stability of nanoparticles is in the regime where the crystal structure of the nanoscale solid is identical to that of the bulk macroscopic solid. In most cases a lower bound for this corresponds to a particle diameter of order 2 nm. For close-packed metals (atomic volume ~14 Å<sup>3</sup>) this is equivalent to a spherical particle containing ~300 atoms, with 200 atoms at the surface of the particle. We contend that the predictions of thermodynamics as applied to the behavior of such nanometer-scale electrodes should be valid. At yet smaller length scales (“molecular clusters”) many physical and chemical properties are known to display quantum size effects,<sup>1,2</sup> oscillatory behaviors,<sup>3</sup> entropically driven icosohedral ⇌ face-centered-cubic (fcc) phase transformations,<sup>4</sup> etc., as a function of the number of molecules defining the cluster size.

There have only been a few reports in the literature aimed at examining the electrochemical stability of small isolated metallic clusters or particles. One study examined the stability of nanometer-size Cu particles on Au (111) surfaces,<sup>5–7</sup> and another examined Ag particles on highly oriented pyrolytic graphite surfaces.<sup>8</sup> Each of these studies reported an enhanced

stability of the nanoscale particle when compared to the dissolution behavior of the corresponding bulk electrode, and these results were qualitatively rationalized in terms of the possible nonmetallic behavior of these particles resulting from quantum size effects. In the case of the Cu particle study, other research groups suggested that mechanical alloying effects may have been responsible for the observation of enhanced stability.<sup>9–12</sup> In another study, the stability of 8–43 nm diameter Ag particle arrays was examined, which showed a decrease in the dissolution potential with particle size, but the quantitative behavior of these particle assemblies could not be rationalized.<sup>13</sup> Recently we presented results of a combined experimental and first-principles study for the electrochemical stability of Pt particles in acid.<sup>14</sup> Both approaches showed that Pt particles with diameters in the range of 1.2–3.0 nm dissolved by the direct electrochemical dissolution path,  $\text{Pt} \rightarrow \text{Pt}^{2+} + 2\text{e}^-$ , and that the dissolution behavior quantitatively followed that expected on the basis of the Gibbs–Thomson equation. Here we extend this work by examining the behavior of Pt particles over a larger size range and present a new thermodynamic analysis which predicts the electrochemical stability of elemental metal particles as a function of potential and pH. Additionally we show how the analysis can be used to construct particle-

\* Arizona State University.

† Johns Hopkins University.

- (1) Volokitin, Y.; Sinzig, J.; deJongh, L. J.; Schmid, G.; Vargaftik, M. N.; Moiseev, I. I. *Nature* **2006**, *384*, 621–623.
- (2) Fan, R.-F.; Bard, A. J. *Science* **1997**, *277*, 1791–1793.
- (3) Henglein, A. *J. Phys. Chem.* **1993**, *97*, 5457–5471.
- (4) Howie, A.; Marks, L. D. *Philos. Mag. A* **1984**, *49*, 95–109.
- (5) Kolb, D. M.; Ullmann, R.; Will, T. *Science* **1997**, *275*, 1097–1099.
- (6) Kolb, D. M.; Engelmann, G. E.; Ziegler, J. C. *Angew. Chem., Int. Ed.* **2000**, *39*, 1123–1125.
- (7) Kolb, D. M.; Simeone, F. C. *Electrochim. Acta* **2005**, *50*, 2989–2996.
- (8) Ng, K. H.; Liu, H.; Penner, R. M. *Langmuir* **2000**, *16*, 4016–4023.

- (9) Nielinger, M.; Baltruschat, H. *Chem. Phys. Chem.* **2003**, *4*, 1022–1024.
- (10) Del Popolo, M.; Leiva, E.; Kleine, H.; Meier, J.; Stimming, U.; Mariscal, M.; Schmickler, W. *Appl. Phys. Lett.* **2002**, *81*, 2635–2637.
- (11) Del Popolo, M.; Leiva, E.; Mariscal, M.; Schmickler, W. *Nanotechnology* **2003**, *14*, 1009–1013.
- (12) Maupai, S.; Dakkouri, A. S.; Strattmann, M.; Schmuki, P. *J. Electrochem. Soc.* **2003**, *150*, C111–C114.
- (13) Ivanova, O. S.; Zamborini, F. P. *J. Am. Chem. Soc.* **2010**, *132*, 70–72.
- (14) Tang, L.; Han, B.; Persson, K.; Friesen, C.; He, T.; Sieradzki, K.; Ceder, G. *J. Am. Chem. Soc.* **2010**, *132*, 596–600.

size-dependent potential–pH diagrams, which previously have only been attempted using first-principles-based electronic structure calculations.<sup>14,15</sup>

Size effects or capillarity in fluid/fluid systems are well known and understood. For example, mechanical equilibrium dictates that there must be a pressure difference between the interior of a spherical liquid drop of radius  $r$  and the pressure of its vapor required to keep this drop from evaporating or growing. This pressure difference, known as the Laplace pressure, is given by  $\gamma(2/r)$ , where  $\gamma$  is the interfacial free energy of the liquid/vapor interface. These considerations lead to the well-known Kelvin equation that describes how the equilibrium vapor pressure of a fluid drop depends on size. Similar considerations for a finite-size solid immersed in a fluid containing a single soluble component of the solid are poorly understood, despite the fact that Gibbs considered this in some detail and developed the conditions for this equilibrium.<sup>16</sup> A major source of this misunderstanding is related to the Laplace pressure for a solid sphere (assumed isotropic), which is given by  $f(2/r)$ , where  $f$  is the surface stress. We note that, in the case of liquids,  $f = \gamma$ , while for real solids this is rarely the case. This difference in the Laplace pressure for a finite-size solid and a liquid leads to Gibbs's remarkable result that at equilibrium there is a difference in the chemical potential of the component in the solid and fluid phases, given by

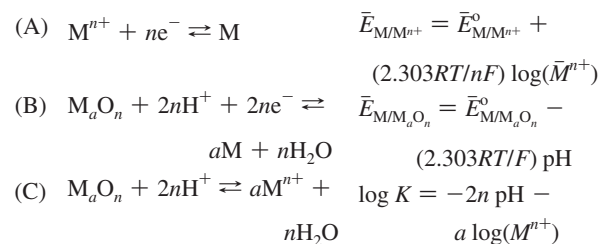
$$\mu_s - \mu_l = (f - \gamma)\Omega(2/r) \quad (1)$$

where  $\Omega$  is the molar volume of the solid. Note that, for equilibrium between a planar solid surface ( $r \rightarrow \infty$ ) and a fluid or for fluid/fluid systems ( $f = \gamma$ ), the standard equilibrium condition,  $\mu_s = \mu_l$ , is recovered.

While eq 1 and its consequences were discussed in detail by Cahn,<sup>17</sup> he did not present a complete derivation. In the Supporting Information we do so, following a procedure similar to that used by Cammarata.<sup>18</sup> Cahn and Cammarata also discussed the generalization of this equilibrium condition to multicomponent solids, and, as Cammarata has pointed out, the surface free energy has to be interpreted as the open surface availability.<sup>19</sup>

In the case of elemental metal stability, the electrochemical and chemical equilibria that we consider are represented by the following set of equations:

- (15) Taylor, C. D.; Neurock; Scully, J. R. *J. Electrochem. Soc.* **2008**, *155*, C407–C414.
- (16) Gibbs, J. W. *The Collected Works of J.W. Gibbs*; Longmans: Green, NY, 1906; Vol. 1, pp 317–318; reprinted Ox Bow Press: Woodbridge, CT, 1993.
- (17) Cahn, J. W. *Acta Metall.* **1980**, *28*, 1333–1338.
- (18) Cammarata, R. C. *Philos. Mag.* **2008**, *88*, 927–948.
- (19) For a multicomponent solid/fluid interface  $\gamma$  is not well defined since the dividing surface can be set so as to make the surface excess of only one component zero. Since the surface excess of the other components will in general be non-zero, the chemical potential of these components on the surface enter into the definition of  $\gamma$  (see eq S2, Supporting Information). These chemical potentials are in general non-uniform and so ill-defined. The concept of surface availability is associated with the minimum work to create a surface. In analogy with eq S2, it is defined as  $\sigma = (U^2 - TS^2 - \sum_i \mu_i n_i^2)/A$ , where  $\mu_i$  is the chemical potential of component  $i$  in the fluid reservoir. Notionally  $\sigma$  may be viewed as a simple re-interpretation of  $\gamma$ , and other than this note we will not distinguish between these quantities herein.



In these equations  $K$  is the equilibrium constant, and the standard potentials and metal ion concentrations defining equilibrium for planar surfaces are indicated by the designations  $\bar{E}$  and  $\bar{M}^{n+}$ . In what follows we will develop the Gibbs–Thomson relation for each of these reactions for a spherical nanoparticle assuming isotropic surface energy and surface stress.

First consider reaction (A), involving the reversible electro-dissolution or deposition of  $M$ . If  $\bar{M}^{n+}$  is the saturation concentration for a planar surface as defined in (A), the chemical potential of the metal cation in the liquid phase at concentration  $M^{n+}$  surrounding a finite size particle is  $\mu_l = \bar{\mu}_l(\bar{M}^{n+}) + RT \ln(M^{n+}/\bar{M}^{n+})$ , and the chemical potential of the metal in the nanoparticle is  $\mu_s = \bar{\mu}_l(\bar{M}^{n+}) + f_M \Omega_M(2/r)$ . In these equations  $\bar{\mu}_l(\bar{M}^{n+})$  is the chemical potential of the metal cation in the liquid phase in equilibrium with the planar solid surface at chemical potential  $\bar{\mu}_s(\bar{M}) = \bar{\mu}_l(\bar{M}^{n+})$ . Applying the equilibrium condition (eq 1), we obtain

$$RT \ln(M^{n+}/\bar{M}^{n+}) = \gamma_M \Omega_M(2/r) \quad (2)$$

The left-hand side of this equation is the Gibbs free energy difference for the liquid phase surrounding a spherical particle of radius  $r$  and a planar surface ( $r \rightarrow \infty$ ),  $\Delta G_l = G_l(r) - \bar{G}_l$ . Since  $\Delta G = -nFE$ ,

$$E_{M/M^{n+}(r)} - \bar{E}_{M/M^{n+}} = -\frac{\gamma_M \Omega_M}{nF}(2/r) \quad (3)$$

Next consider reaction (C) for a nanoparticle, describing the chemical equilibrium between the metal oxide and dissolved metal cations in the electrolyte. The chemical potential of  $M_aO_n$  in the solid in equilibrium with the liquid is  $\mu_s = \bar{\mu}_l(\bar{M}^{n+}) + f_{M_aO_n/M} \hat{\Omega}_{M_aO_n}(2/r)$  and the chemical potential of  $M^{n+}$  in the liquid phase is  $\mu_l = \bar{\mu}_l(\bar{M}^{n+}) + RT \ln(M^{n+}/\bar{M}^{n+})$ . Applying the equilibrium condition (eq 1), we obtain

$$RT \ln(M^{n+}/\bar{M}^{n+}) = [\gamma_{M_aO_n/M} \langle \Omega_{M_aO_n/M} \rangle + f_{M_aO_n/M} (\hat{\Omega}_{M_aO_n} - \langle \Omega_{M_aO_n/M} \rangle)](2/r) \quad (4)$$

In this expression the subscript  $M_aO_n/M$  refers to the value of the parameter for the “oxide-covered” particle (see Supporting Information). The first term in brackets on the right-hand side of the equation reflects the fact that, as the oxide dissolves (or accretes) from the particle surface, there is work done associated with an area change, and the second term describes the excess work done against the surface stress owing to the difference between the partial molar volume of  $M_aO_n$ ,  $\hat{\Omega}_{M_aO_n}$ , and the average molar volume,  $\langle \Omega_{M_aO_n/M} \rangle$ , of the nanoparticle.

The standard potential for the formation of the metal oxide is obtained by using eqs 3 and 4 in a manner analogous to that using eqs (A) and (C) to obtain eq (B):

$$E_{M_aO_n/M} - \bar{E}_{M_aO_n/M} = \left[ \frac{\gamma_{M_aO_n/M} \langle \Omega_{M_aO_n/M} \rangle}{nF} + \frac{f_{M_aO_n/M}}{nF} (\hat{\Omega}_{M_aO_n} - \langle \Omega_{M_aO_n/M} \rangle) - \frac{\gamma_M \Omega_M}{nF} \right] (2/r) \quad (5)$$

Equations 3 and 5 represent thermodynamic predictions for the effect of particle size on the shift in the standard equilibrium potentials of reactions (A) and (B). For small enough metal nanoparticles the entire particle may be oxidized, and in this case the surface stress term in eqs 4 and 5 will be 0. In considering the equilibrium of nanometer-scale Pt particles, Darling and Meyers obtained an equation similar to eq 5, except that the surface stress term was absent.<sup>20</sup>

The standard potentials are well defined only if the nanoparticles have the equilibrium shape defined by the Wulff construction.<sup>21</sup> Since real particles rarely take on equilibrium shapes, in comparing experimental results to these predictions, these equations should be considered as dissolution and oxidation potentials rather than formal equilibrium potentials. In the experiments discussed below, since the nanoparticle shapes were generally ellipsoidal, we have chosen to replace the factor of  $(2/r)$  with  $1/r_1 + 1/r_2 (= 2/r_m)$ , where  $r_1$  and  $r_2$  correspond to half the length of the major and minor axes of the ellipsoid-shaped particle, respectively.<sup>22</sup> The values chosen for  $f$  and  $\gamma$  reflect the surface orientations that dominate the particle shape.

The quantities that we require in order to develop simple particle-size-dependent potential–pH diagrams using eqs (A)–(C) include  $\gamma_M$ ,  $\gamma_{M_aO_n/M}$ , and  $f_{M_aO_n/M}$ . Today, these parameters are most reliably determined by first-principles-based density functional calculations. While there are relatively numerous such calculations for the metals, to our knowledge a similar situation does not currently exist for the values of these parameters in the case of metal oxides. There are few values for the surface energy of the monolithic metal oxides and yet fewer values for the surface energy of an oxide covering a metal surface. The values that are available seem to have been primarily motivated by applications such as catalysis, for which the oxides of Pt<sup>23–25</sup> and Ti<sup>26–28</sup> have received particular attention. After some careful examination, we do not feel justified in constructing a particle-size-dependent potential–pH diagram for Ti, owing to the multitude of lower energy oxides that form on Ti prior to  $TiO_2$ . In the discussion that follows we focus on the case of Pt.

In principle, in the case of the surface stress,  $f_{M_aO_n/M}$ , wafer curvature measurements can be made in order to measure the change in surface stress,  $\Delta f$ , that occurs when the bare metal forms the oxide, allowing for the determination of this parameter through  $f_{M_aO_n/M} = f_M + \Delta f$ . Such a  $\Delta f$  measurement may encompass a variety of adsorption/desorption phenomena that

- (20) Darling, R. M.; Meyers, J. P. *J. Electrochem. Soc.* **2003**, *150*, A1523–A1527.
- (21) Cahn, J. W.; Carter, W. C. *Metall. Trans. A* **1996**, *27*, 1431–1440.
- (22) We examined several different measures defining an average or effective mean particle radius and found that, over the range of particle sizes investigated,  $r_m$  is rather insensitive to the particular scheme adopted.
- (23) Seriani, N.; Mittendorfer, F. *J. Phys.: Condens. Matter.* **2008**, *20*, 184023.
- (24) Seriani, N.; Jin, Z.; Pompe, W.; Ciacchi, L. C. *Phys. Rev. B* **2007**, *76*, 155421.
- (25) Seriani, N.; Pompe, W.; Ciacchi, L. C. *J. Phys. Chem. B* **2006**, *110*, 14860–14869.
- (26) Lazzari, M.; Vittadini, A.; Selloni, A. *Phys. Rev. B* **2001**, *63*, 155409.
- (27) Lazzari, M.; Vittadini, A.; Selloni, A. *Phys. Rev. Lett.* **2001**, *87*, 266105.
- (28) Kamisaka, H.; Yamashita, K. *Surf. Sci.* **2007**, *601*, 4824–4836.

**Table 1.** Parameter Values Used in the Evaluation of  $E_{Pt/Pt^{2+}}$  (Eq 3') and  $E_{PtO/Pt}$  (Eq 5')

parameter	value	method or measurement
$\gamma_{Pt}$	2.4 J/m <sup>2</sup>	first-principles calculation <sup>30</sup>
$\gamma_{PtO/Pt}$	0.5 J/m <sup>2</sup>	first-principles calculation <sup>25</sup>
$f_{Pt}$	5.6 J/m <sup>2</sup>	first-principles calculation <sup>31</sup>
$f_{PtO/Pt}$	3.0 J/m <sup>2</sup>	measurement of $\Delta f$ using wafer curvature <sup>a</sup>
$\Omega_{Pt}$	$9.09 \times 10^{-6}$ m <sup>3</sup>	unit cell
$\hat{\Omega}_{PtO}$	$1.49 \times 10^{-5}$ m <sup>3</sup>	unit cell <sup>32</sup>
$\langle \Omega_{PtO/Pt} \rangle$	$1.08 \times 10^{-5}$ m <sup>3</sup>	mean value for a Pt particle 2.0–5.0 nm in radius

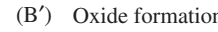
<sup>a</sup> See Supporting Information.

occur during oxide formation (e.g.,  $SO_4^{2-}$  adsorption during formation of  $PtO/Pt$  in sulfuric acid); however, it seems likely that such adsorbates are replaced in the process of oxide formation. Nevertheless, if  $\Delta f$  is measured in the same electrolyte as that for which particle stability is examined, the determination of  $f_{M_aO_n/M}$  will necessarily include such effects. In the case of Pt, we used wafer curvature to determine  $f_{PtO/Pt}$  in 0.1 M  $H_2SO_4$  (see Supporting Information).

The analogues of eqs (A)–(C) for the case of Pt are



$$Pt^{2+} + 2e^- \rightleftharpoons Pt \quad E_{Pt/Pt^{2+}} = 1.188 + 0.0295 \log(Pt^{2+})$$



$$PtO + 2H^+ + 2e^- \rightleftharpoons Pt + H_2O \quad E_{Pt/PtO} = 0.980 - 0.059 \text{ pH}$$



$$PtO + 2H^+ \rightleftharpoons Pt^{2+} + H_2O \quad \log(Pt^{2+}) = -7.06 - 2\text{pH}$$

Since the (111) orientation is known to dominate the surface structure of Pt nanoparticles,<sup>29</sup> we have used first-principles values for  $\gamma_{Pt}$  and  $f_{Pt}$  for (111) oriented Pt surfaces. Table 1 shows the parameter values used for the thermodynamic prediction for the dissolution potentials as a function of particle size (see Supporting Information). Assuming a  $Pt^{2+}$  concentration in the electrolyte of  $10^{-6}$  M, we obtain the following numerical equations corresponding to eqs 3 and 5:

$$E_{Pt/Pt^{2+}} = 1011 - 113(2/r_m) \quad (3')$$

$$E_{PtO/Pt} = 922 - 21(2/r_m) \quad (5')$$

where the voltages are in millivolts (vs normal hydrogen electrode (NHE)) and  $r_m$  is in units of nanometers. These results allow us to develop a particle-size-dependent potential–pH diagram taking into consideration only the solids Pt and  $PtO$  and the dissolved species  $Pt^{2+}$ . Figure 1 shows this diagram for particles ranging from 1 to 10 nm in diameter.

Equations 3' and 5' predict that a change in dissolution mechanism should occur for  $r_m \approx 2$  nm. For smaller particles dissolution should occur via the direct electrodissolution mechanism,  $Pt \rightarrow Pt^{2+} + 2e^-$ , and follow the behavior predicted by eq 3'. Larger particles are predicted to form  $PtO$  which subsequently chemically dissolve. In an earlier publication, we investigated the electrochemical stability of individual Pt particles with  $r_m$  in the range of 0.6–1.5 nm using electrochemical scanning tunneling microscopy (ECSTM), and the results were in excellent agreement with eq 3'.<sup>14</sup> Here, following similar protocols, we present results over a larger range of particle size.

(29) Sattler, M. L.; Ross, P. N. *Ultramicroscopy* **1986**, *20*, 21–28.

(30) Da Silva, J. L. F.; Stampfl, C.; Scheffler, M. *Surf. Sci.* **2006**, *600*, 703–715.

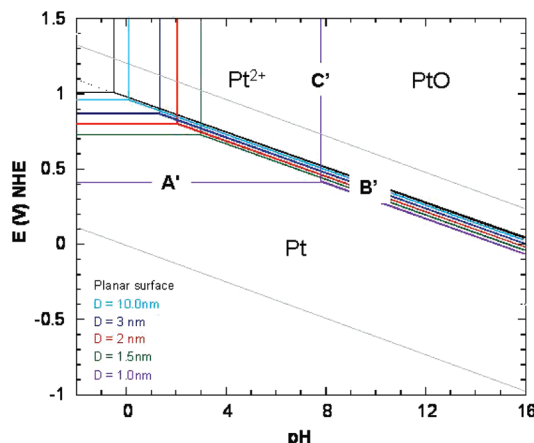


**Figure 1.** Particle-size-dependent potential–pH diagram for  $\text{Pt}/10^{-6}$  M  $\text{Pt}^{2+}$ . The separation for forming  $\text{PtO}$  for a planar surface (black line) and the  $D = 1.0$  nm diameter particle,  $E_{\text{PtO}/\text{Pt}}(r = 0.5 \text{ nm}) - E_{\text{PtO}/\text{Pt}}$ , is 42 mV (exaggerated in this diagram for the purpose of clarity). Reaction labels correspond to those in the text.

Briefly, the stability of individual Pt-black particles was examined in aerated 0.1 M  $\text{H}_2\text{SO}_4$ . The agglomerated Pt-black particles were characterized using transmission electron microscopy, energy-dispersive analysis, and X-ray scattering.<sup>14</sup> In order to obtain individual particles, these agglomerates were ultrasonicated in isopropyl alcohol and dispersed onto a  $\text{Ag}_{0.05}\text{Au}_{0.95}$  {111} textured thin-film surface. In earlier work we employed a pure gold {111} textured thin film and a deposition protocol in order to avoid the  $\sqrt{3} \times 22$  surface reconstruction that, when lifted at  $\sim 0.55$  V vs NHE, results in the formation of variously sized gold islands on the surface, which made substrate preparation tedious.<sup>14</sup> We found that a more convenient route to avoid the reconstruction was the addition of 5 atom % Ag to the Au thin film and, in ancillary ECSTM experiments, determined that this alloy surface was stable in 0.1 M  $\text{H}_2\text{SO}_4$  to  $\sim 1.2$  V vs NHE.

Figure 2 shows an ECSTM image of about 35 individual Pt-black particles in 0.1 M  $\text{H}_2\text{SO}_4$ . A voltage of 350 mV was maintained on the electrode until stable imaging was established. The potential was then gradually increased to 650 mV and subsequently pulsed in 50 mV increments and held for a period of time, as shown in Figure 2A. Finally the potential was pulsed back to 650 mV. Analysis involved examining the collected set of images at higher magnification in order to measure particle sizes and evaluate particle stability. All of the images shown in Figure 2B–L correspond to those obtained at the end of the temporal hold time at the given potential. Figure 2E–H shows magnified views of frame 5 of Figure 2B, containing four particles ranging in size ( $r_m$ ) from 1.9 to 3.5 nm. Generally we observed that the rate of particle dissolution decreased significantly with increasing particle size for particles larger than  $\sim 2$  nm in radius. Smaller particles virtually always disappeared within the  $\sim 150$  s required to obtain a topographic image, while larger particles survived for much longer. We suggest this qualitative difference in dissolution rate implies that different dissolution mechanisms operate for the large and small particles. The largest particle in this frame was still present after  $\sim 30$  min at 1200 mV. Close inspection of the images of the larger particles also reveals that during dissolution there is a tendency

for particles to develop rather well-defined facets. For example, Figure 2G shows that particle 3 in frame 5 of Figure 2B develops  $\langle 110 \rangle$  edge facets, as might be expected for a fcc particle since this family of step orientations has the lowest energy and therefore dissolves slowest. Figure 2I–L shows magnified views of an ECSTM image, frame 6 of Figure 2B, showing three Pt-black particles ranging in size ( $r_m$ ) from 2.7 to 7.2 nm. The smaller particles both dissolve at 950 mV, while the large particle was stable in both size and shape throughout the entire potential–time sequence. We have highlighted the shape of the large particle in panels I, K, and L as a guide to the eye, demonstrating its stability.

Figure 3 shows the dependence of particle size on potential together with eqs 3' and 5'. This figure also includes the data set from our prior publication.<sup>14</sup> While it is apparent that the agreement between experiment and the thermodynamic prediction is good, we discuss potential sources of error in both the experiment and the thermodynamic analysis.

The major source of experimental error results from our inability to accurately determine the potential at which some of the large particles oxidize. Smaller particles almost always disappeared from the ECSTM image over the time period of a single scan, and so the dissolution potential was well defined within the potential step sequence of the experiments. Larger particles dissolved more slowly, often becoming qualitatively smaller over many scans either at a single potential or over a sequence of potential steps. We tried several different protocols to assess changes in particle size (e.g., 20–50% reductions in  $r_m$ ), but for some particles this assessment was complicated by changes in particle shape which often involved the development of well-defined  $\langle 110 \rangle$  facets. Consequently, for a number of these particles “dissolution potentials” could not be determined. Equation 5' defines an oxidation potential, and we assume in our data analysis that the potential at which a particle gets smaller is strongly correlated to this oxidation potential. Consequently, the potentials defined for the larger particles (blue points in Figure 3) likely represent upper bounds for the particle-size-dependent reaction:  $\text{Pt} + \text{H}_2\text{O} \rightarrow \text{PtO} + 2\text{H}^+ + 2\text{e}^-$ .

There are two potential sources of error in the analysis we have used in comparing the experimental results to the thermodynamic prediction. One derives from the accuracy of the first-principles calculations that we have used for  $\gamma_{\text{Pt}}$ ,  $\gamma_{\text{PtO}/\text{Pt}}$ , and  $f_{\text{Pt}}$ . In examining the literature, we have found that there can be considerable variation in the values of the surface stress and surface energy calculated for metals, depending on the nature of the approximation (e.g., LDA or GGA) and its implementation in density functional theory.<sup>30</sup> These different approximations often result in values for surface parameters that can vary by as much as 15%. Our determination of  $f_{\text{PtO}/\text{Pt}}$  is based on the first-principles value of  $f_{\text{Pt}}$  and the experimentally measured  $\Delta f$  upon forming an oxide on  $\text{Pt}(111)$ . The  $\Delta f$  that we measure is within  $\sim 10\%$  of that calculated by Feibelman for one-fourth of an adsorbed oxygen monolayer on  $\text{Pt}(111)$  [i.e.,  $\text{O}(2 \times 2)/\text{Pt}(111)$ ].<sup>33</sup> Another source of error relates to our prediction of  $E_{\text{PtO}/\text{Pt}}$ , since the exact structure and composition of the oxide that forms on a planar  $\text{Pt}(111)$  surface in 0.1 M  $\text{H}_2\text{SO}_4$  are not known. We have assumed a stoichiometric  $\text{PtO}$  oxide with a crystal structure reflecting that of bulk  $\text{PtO}$ , but more than likely the oxide is not stoichiometric. Nevertheless, the first-principles calculations that do exist have considered various platinum oxide forms, and many of these have surface

(31) Needs, R. J.; Mansfeld, M. *J. Phys.: Condens. Matter* **1989**, *1*, 7555–7563.

(32) McBride, J. R.; Graham, G. W.; Peters, C. R.; Weber, W. H. *J. Appl. Phys.* **1991**, *69*, 1596–1604.

(33) Feibelman, P. J. *Phys. Rev. B* **1997**, *56*, 2175–2182.

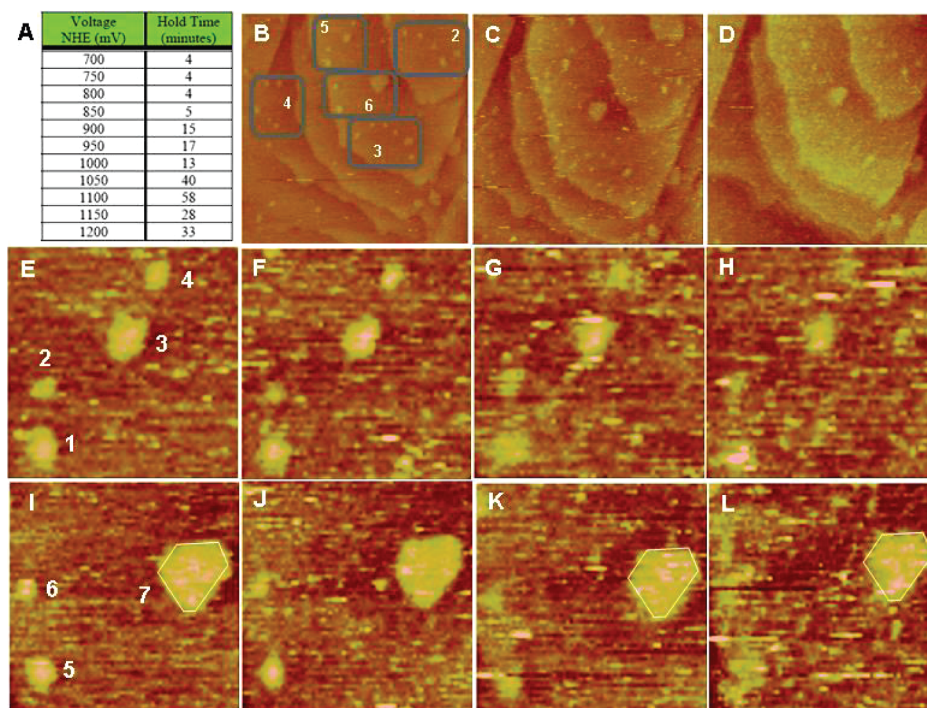


**Figure 2.** ECSTM topographic height mode images showing Pt-black particles on a  $\text{Au}_{0.95}\text{Ag}_{0.05}$  {111} surface in 0.1 M  $\text{H}_2\text{SO}_4$ . These particles were subjected to 50 mV potential steps for the hold times shown in panel A. (B)–(D) Images of the sample over a scan size of  $178 \times 178$  nm at potentials of (B) 650, (C) 1050, and (D) 650 mV after the potential step protocol shown in (A). (E)–(H) Magnification of the ECSTM images in frame 5 of panel B; scan size  $40 \times 40$  nm. (E) At 650 mV, the mean radii of the particles present in this image are as follow: particle 1,  $r_m = 2.5$  nm; particle 2,  $r_m = 1.90$  nm; particle 3,  $r_m = 3.5$  nm; particle 4,  $r_m = 2.2$  nm. (F) At 900 mV, particles 2 is dissolving while particles 1, 3, and 4 are stable. (G) At 1050 mV, all the particles are undergoing shape change and/or becoming smaller. (H) At 1100 mV, particles 2 and 4 have disappeared while particles 1 and 3 are still present, albeit smaller in size. At 1200 mV (not shown), particle 1 disappears while a remnant of particle 3 remains. (I)–(L) Magnification of ECSTM images in frame 6 of panel B; scan size  $48 \times 48$  nm. (I) At 650 mV, the mean radii of the particles present in this image are as follow: particle 5,  $r_m = 3.1$  nm; particle 6,  $r_m = 2.7$  nm; particle 7,  $r_m = 7.2$  nm. (J) At 950 mV, particle 6 began dissolving at 900 mV (not shown); particle 5 has just started to dissolve while for particle 7 there is no significant change in shape or size. (K) At 1050 mV, particles 5 and 6 have virtually disappeared while particle 3 is stable. (L) At 1200 mV, particle 7 remained stable in both size and shape throughout the potential–time protocol of the experiment. The shape of this particle is highlighted in panels I, K, and L as a guide to the eye.

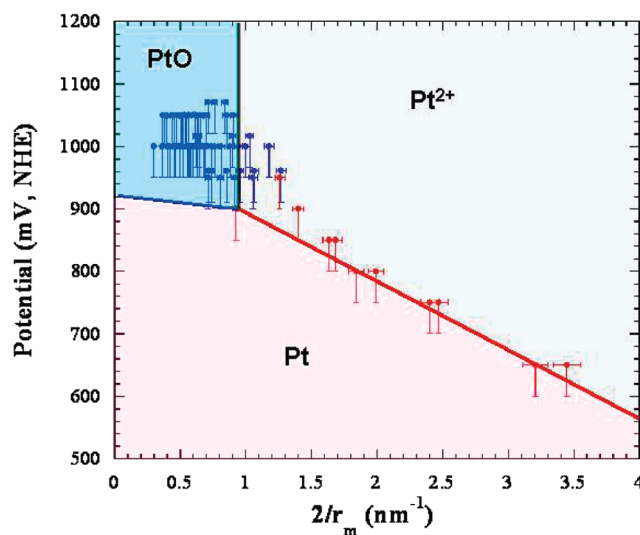


**Figure 3.** Influence of the Pt particle size ( $2/r_m$ ) on the dissolution and oxidation potentials. The red line is eq 3', and the blue line is eq 5'. A linear fit to the data (red points) yields  $V_{\text{diss}} = 1051 - 122(2/r_m)$  mV, which should be compared to eq 3'. These points were selected for the fit as they represent those particles that disappeared within a single ECSTM image scan. The blue points correspond to those particles that formed an oxide and followed a chemical dissolution route.

energies of  $0.5 \pm 0.2$  J  $\text{m}^{-2}$ .<sup>25</sup> This small range in  $\gamma_{\text{PtO}/\text{Pt}}$  has little effect on the predictions expressed by eq 5'.

We have presented a general thermodynamic analysis for the effect of particle size on the standard potentials defining elemental metal/metal ion equilibrium and metal/metal oxide equilibrium and have used the analysis to construct a particle-size-dependent potential–pH diagram for the case of Pt nanoparticles. Unfortunately, the current database for such calculations requires values of the surface energy and surface stress for metal oxides, and these are presently not available for any other system to our knowledge. This is a situation that can be remedied, and we are hopeful that more first-principles-based calculations for these parameters will become available in the future which will allow for the development of particle-size-dependent potential–pH diagrams for any elemental metal of interest.

**Acknowledgment.** K.S. and C.F. acknowledge support from the Center for Renewable Energy Electrochemistry at Arizona State University and the National Science Foundation (DMR-0855969 and DMR-0301007). R.C.C. acknowledges support from the National Science Foundation (DMR-0706178).

**Supporting Information Available:** Derivation of eq 1, experimental methods for determination of  $f_{\text{PtO}/\text{Pt}}$  using wafer curvature, discussion of the average molar volume of the oxide-covered Pt nanoparticle, and supplemental Figures S1 and S2. This material is available free of charge via the Internet at <http://pubs.acs.org>.

JA104421T